This document is the accepted manuscript version of the following article:

Finizio, S., Bailey, J. B., Olsthoorn, B., & Raabe, J. (2022). Periodogram-based detection of unknown frequencies in time-resolved scanning transmission X-ray microscopy. ACS Nano. https://doi.org/10.1021/acsnano.2c08874

Periodogram-based detection of unknown frequencies in time-resolved scanning transmission X-ray microscopy

Simone Finizio,*,† Joe Bilko Bailey,†,¶ Bart Olsthoorn,‡ and Jörg Raabe†

†*Paul Scherrer Institut, 5232 Villigen PSI, Switzerland*

‡*Nordita, KTH Royal Institute of Technology and Stockholm University, Hannes Alfvéns väg 12, SE-106 91 Stockholm, Sweden*

¶*Institut de Physique, EPFL, 1015 Lausanne, Switzerland*

E-mail: simone.finizio@psi.ch

Abstract

Pump-probe time-resolved imaging is a powerful technique that enables the investigation of dynamical processes. Signal-to-noise and sampling rate restrictions normally require that cycles of an excitation are repeated many times with the final signal reconstructed using a reference. However, this approach imposes restrictions on the types of dynamical processes that can be measured, namely that they are phase locked to a known external signal (e.g. a driven oscillation or impulse). This rules out many interesting processes such as auto-oscillations and spontaneously forming populations e.g. condensates. In this work we present a method for time-resolved imaging, based on the Schuster periodogram, that allows for the reconstruction of dynamical processes where the intrinsic frequency is not known. In our case we use time of arrival detection of X-ray photons to reconstruct magnetic dynamics without using *a-priori* information

on the dynamical frequency. This proof of principle demonstration will allow for the extension of pump-probe time-resolved imaging to the important class of processes where the dynamics are not locked to a known external signal and in its presented formulation can be readily adopted for x-ray imaging and also adapted for wider use.

Keywords

time-resolved imaging, magnetic microscopy, scanning transmission X-ray microscopy, Schuster periodogram, auto-oscillatory dynamics

Pump-probe time-resolved (TR) X-ray microscopy is a powerful technique that allows for the investigation of several dynamical processes occurring at the nanometer and nanosecond scales. Thanks to the X-ray magnetic circular dichroism effect[1], which provides a contrast mechanism sensitive to the local orientation of the spins in a ferromagnetic system, TR investigation of magneto-dynamical processes is possible.

Amongst the various pump-probe TR X-ray microscopy techniques, scanning transmission X-ray microscopy (STXM) has been often utilized for the study of magneto-dynamical processes[2–5]. In STXM imaging, a monochromatic X-ray beam is focused by a diffractive lens onto a nanometric spot on an X-ray transparent sample, and the transmitted intensity is recorded by a point detector such as an avalanche photodiode or a photomultiplier tube. To obtain an image, the sample is raster scanned with a piezoelectric stage[6].

TR-STXM allows for the investigation of pump-probe dynamics by employing an avalanche photodiode (APD) as X-ray detector. APDs with bandwidths higher than the bunch repetition rate of the synchrotron light source (in the case of the Swiss Light Source, about 500 MHz) can be easily sourced commercially, allowing for the possibility to resolve X-ray photons originating from neighboring electron bunches. By utilizing a voltage discriminator unit combined with a demultiplexer locked to the synchrotron master clock, APD counts can be sorted in specific counters depending on the electron bunch from which they generated, and a time-series can be reconstructed[7].

However, this approach has two main limitations, given by the fact that the excitation frequencies that can be probed have to be a fractional multiple of the master clock frequency, and that it is assumed that the X-ray photons are generated exactly at the center of the electron bunch. This second assumption limits the maximum temporal resolution of the technique to the width of the electron bunches, which are on the order of 70-100 ps full-width at half-maximum (FWHM) in normal optics operation[8]. Both of these limitations can be lifted by directly measuring the time-of-arrival of the X-ray photons at the APD, by means of a time-to-digital converter[8]. This setup is sketched in Fig. 1(a). The time-to-digital converter (QuTAG from QuTools GmbH) provides an absolute time stamp corresponding to the moment when an input signal crosses a user defined voltage threshold. To overcome the unwanted jitter in the detection time caused by the distribution of amplitudes of the single voltage pulses generated by the APD, a software constant-fraction-discrimination protocol has been implemented. This process is based on the acquisition of the time at which the APD pulse crosses a user-defined voltage threshold at its rising and falling edges, and calculating the average between the two times, as depicted in Fig. 1(b). To perform this measurement, the signal from the APD is split and recorded by two separate channels of the time-to-digital converter[8].

In addition to the measurement of the arrival time of the X-ray photons, a marker channel is also utilized in the standard implementation of the setup. The marker signal is a pulsed signal synchronized with the excitation being investigated (e.g. in the case of a magnetic vortex gyration process, the marker signal would be a pulse with the same period of the radio-frequency - RF - signal used to excite the dynamical process). With this marker, the measured arrival times of the X-ray photons can be sorted based on the time difference between the X-ray photon arrival time and the time at which the last marker pulse was recorded. This concept is sketched in Fig. 2(a). Finally, a time series for each pixel of the TR-STXM image can be reconstructed by binning the recorded time differences, as sketched in Fig. 2(b). The width of the time step in the reconstructed time series can be

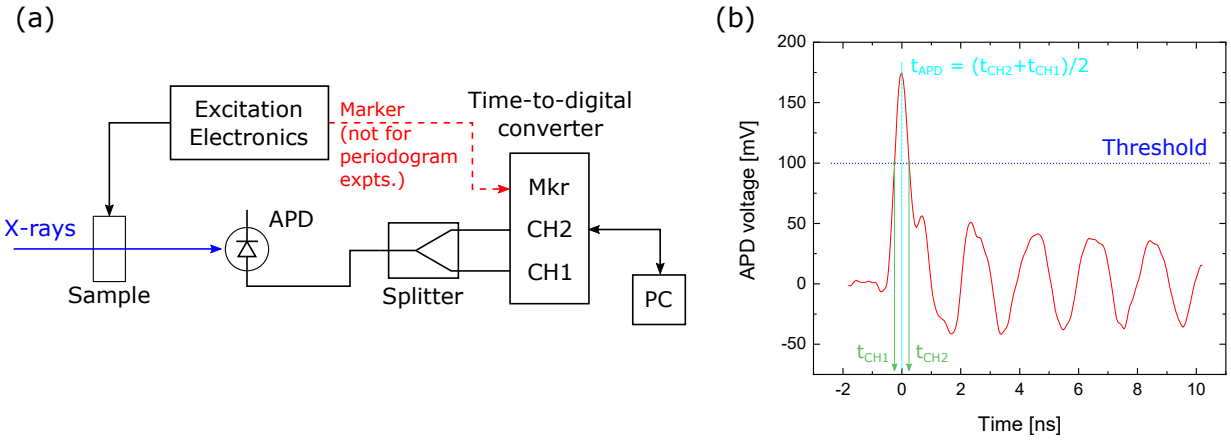

Figure 1: (a) Sketch of the time-of-arrival detection setup utilized for the results reported in this work. The setup is the same as the one described in[8], with the difference that the marker signal provided by the excitation electronics is not considered upon performing the reconstruction (leading to, effectively, a reconstruction where the excitation frequency is not known *a-priori*). (b) Oscilloscope trace of an APD pulse, showing the recording of the arrival time performed by constant fraction discrimination, where the time at which the pulse crosses a user-defined threshold in its rising and falling edges is recorded.

selected by changing the number of equal width bins used in the reconstruction (in the case sketched in Fig. 2, 7 bins were used). For the example shown in Fig. 2(c), for which a video of the reconstructed TR image is available in the supplementary information, a 150 nm thick permalloy ($Fe_{19}Ni_{81}$ - Py) microstructured square of 2×2 μm^2 area was used. The Py microstructure stabilizes a flux-closure Landau state, with a magnetic vortex core at its center[9]. This spin configuration can be excited by a magnetic field oscillating at RF frequencies, which was generated by fabricating a metallic stripline on top of the magnetic microstructure, and injecting a RF current across it[10].

An achievable temporal resolution of 20 ps was demonstrated for the standard optics filling pattern of the Swiss Light Source, providing a substantial improvement compared to the 70-100 ps FWHM widths of the X-ray pulses generated within this operation mode[8].

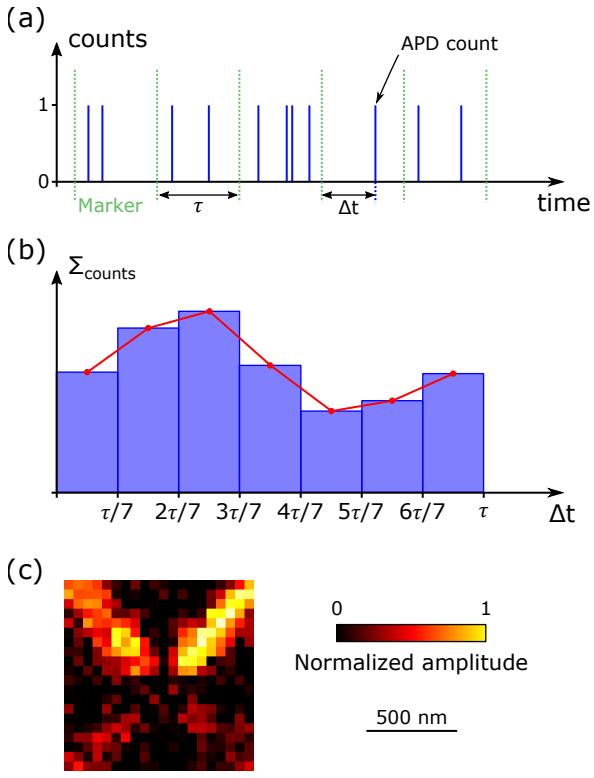

Figure 2: Sketch of the reconstruction process performed in presence of a marker signal. (a) In this method, a marker signal (locked to the excitation signal, with a period τ) is recorded in parallel to the APD pulses, and the time difference Δt between the APD pulse and the last marker is stored. (b) A time trace is calculated by binning together the stored arrival time differences Δt with a user-defined bin size. In the case shown in this sketch, a bin size of $\tau/7$ was chosen, for a total of 7 equal width bins. (c) Heatmap showing the intensity of the dynamics in the magnetic microstructure excited by a 58.825 MHz oscillating in-plane magnetic field.

Results/Discussion

Up to now, TR X-ray microscopy measurements have been performed using a synchronized pump-probe approach, where the time delay between the pumping (e.g. an electrical or optical signal used to excite the dynamical process of interest) and probing (i.e. the single X-ray pulses generated by the light source) signals is known. In our case, this is realized through the marker signal locked to the excitation signal. However, not all dynamical processes are intrinsically locked to an external reference signal, and such processes cannot therefore be imaged through "standard" TR pump-probe microscopy. An example is given by auto-oscillation dynamics, such as those occurring in spin-torque vortex oscillators (STVOs), where the gyration of a magnetic vortex in a specifically tailored heterostructure can be excited by the injection of a DC current across the heterostructure[11]. The gyration frequency is determined by the magnitude of the injected DC current, and is not *a-priori* known, i.e. a timing signal synchronized with the gyration cannot be provided. Other examples of non-phase locked processes include Bose-Einstein Condensates (BEC). A magnon BEC may occur when magnons spontaneously collect and form a coherent population at the minima of the dispersion[12], such populations have wide interest from the magnonics[13], quantum[14] and condensed matter community. Other magnon accumulations can form at magnon-phonon avoided crossings[15], topological and other notable points in a systems dispersion.

In order to allow for the experimental investigation of auto-oscillation processes or, in general, of dynamical processes where a defined, external, timing signal cannot be generated, we present in this work a method for the reconstruction of arbitrary oscillation frequencies from a measurement of only the arrival times of the X-ray photons.

Photon arrival times are unevenly spaced events and appear with a probability that is composed of one or more periodic components. The synchrotron emitting X-ray pulses at roughly 500 MHz is a known component, but there could be other components with unknown frequencies present corresponding to the dynamics of interest. The standard fast Fourier transform (FFT) is not suitable for the non-uniformly and sparsely sampled data, but there

are a number of techniques available for detecting periodicity in such data. For example, a modification to the discrete Fourier transform leads to the Lomb-Scargle periodogram[16,17] that is commonly used for irregular time series within the field of astronomy. The analysis in this work is based on a variant referred to as the *Schuster* (or *classical*) periodogram[18].

The signal S consists of counts at t_n[19],

$$S_{\{t_n\}}(t) = \sum_{n=1}^{N} \delta(t - t_n) \tag{1}$$

where the delta functions appear at a probability that oscillates at the different frequency components that are present. The Schuster periodogram shows the power for each given frequency f in the signal[19]:

$$P(f; t_n) = \left| \sum_{n=1}^{N} e^{-2\pi i f t_n} \right|^2 \tag{2}$$

The usual Nyquist frequency for uniform sampling ($f_{\mathrm{Ny}} = f_s/2$, where f_s is the sampling rate) does not apply here, and signals at much higher frequencies can be identified. Instead, the limit on resolvable frequencies is set by the precision of the time of arrival measurement, which can be formulated as the number of decimal places D used in the time stamps, $f_{\max} = \frac{1}{2}10^D$[19].

In our case, the temporal resolution of the time-to-digital converter is in picoseconds, leading to a theoretical maximum identifiable frequency of $f_{\max} = 0.5\ \mathrm{ps}^{-1} = 0.5$ THz. The width of the peaks reconstructed by the Schuster periodogram would be given by $1/T$, where T is equal to the sampling window length, i.e. the pixel dwell time for a STXM image. In order to resolve the peak in the periodogram, it is necessary to perform a sufficiently dense sampling in the frequency, given by $\Delta f = 1/n_0 T$ where n_0 is the number of samples per peak. A good estimate for n_0 is 5, yielding a Δf of 2 Hz for a typical pixel dwell time of 100 ms. This would imply, if the entire theoretical frequency range of 0.5 THz is investigated, that $N_{\mathrm{eval}} = 5T f_{\max} = 2.5 \cdot 10^{11}$ periodograms would have to be computed. The calculation of 10^{11} periodograms is computationally intractable, meaning that in practice either the pixel

dwell time T or the investigated frequency span $f_{\max}$ have to be limited. One approach that can be utilized to reduce the number of periodograms to compute is that a first estimation of the oscillation frequency of the system under investigation can be made from first principles, simulations, or from measurements with complementary techniques.

The accessible frequency span that can be "blindly" sampled is limited by the available computational capabilities. Through the use of CUDA computation libraries, operating over multiple GPUs, the accessible frequency span within acceptable computational time windows is expected to be on the order of 100-200 MHz, enabling for the search of unknown dynamics over a large frequency range starting from a first principles estimation of the oscillation frequency.

To demonstrate the feasibility of utilizing the Schuster periodogram for reconstructing TR STXM images, we imaged the vortex gyration dynamics of the same Py microstructured element used for obtaining the result shown in Fig. 2(c). For these experiments, a combination of two excitation signals was used: the signal at 58.825 MHz shown in Fig. 2(c), and an additional signal oscillating at 58.5 MHz. Both signals are sinusoidal excitations. To ensure that the two excitation signals do not have a common integer multiple for their periods, we generated them with two independent, free running, arbitrary waveform generators. The two signals were then independently amplified and combined by means of a power combiner. No marker signal was provided to the time-to-digital converter. To verify that the Schuster periodogram is able to detect differences in the magnitude of the excited dynamics, the amplitude of the signal at 58.5 MHz was set to half of that of the signal at 58.825 MHz (i.e. a quarter of the power). The amplitude of the 58.825 MHz signal was set to be the same as the one used for the standard reconstruction shown in Fig. 2(c), which was then used as benchmark for the images reconstructed with the Schuster periodogram.

A STXM image of 20×20 pixels centered on the vortex core was acquired with a pixel dwell time of 200 ms. The time of arrival of each X-ray photon was recorded by the time-to-digital converted and stored for the subsequent processing required for the calculation of

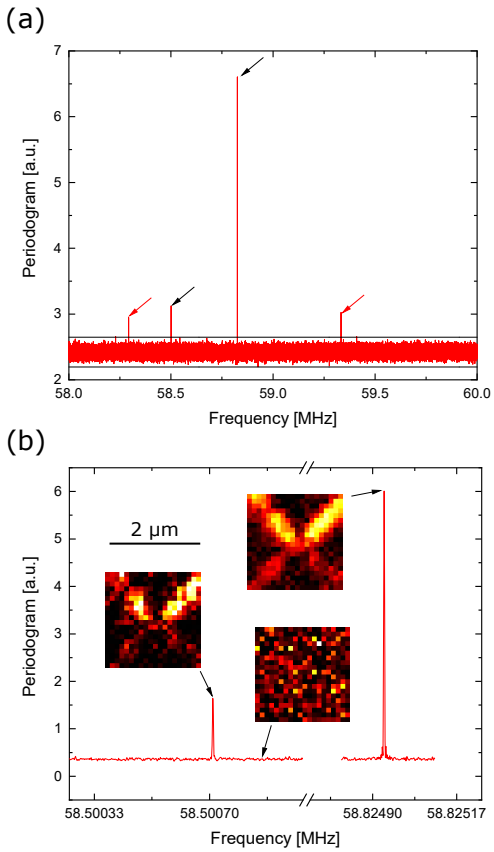

Figure 3: Schuster periodogram from TR-STXM data. (a) Coarse sweep over a 2 MHz interval, step of 20 Hz, calculated by averaging 6 periodograms obtained with different subsets of the data, all corresponding to an effective pixel dwell time of 12.5 ms. Four peaks clearly above the 4σ threshold (marked by the black lines) can be observed, marked by the arrows in the figure. The peaks marked by the red arrows at frequencies of 58.2924 MHz and 59.3333 MHz are aliases of the periodogram peak occurring at 1.0409 MHz caused by the filling pattern structure of the SLS. (b) Fine sweep over a 1 kHz interval around the two peaks discovered in the coarse search, step of 1 Hz, pixel dwell time of 200 ms (full dataset). The inset figures show the reconstructed amplitude of the excitation at the frequencies indicated by the black arrows. Note here that the excitation power for the 58.5 MHz signal was a quarter of that at 58.825 MHz.

the Schuster periodogram. A total of about 10^6 events per pixel was recorded. The data was processed using a CUDA script operating on a NVidia GTX 1080 Ti GPU. Using the frequency sweep settings described in the next paragraphs, a processing time of about 5-10 minutes was required for the calculation of the image periodogram. Future upgrades on the computational side, which will enable to distribute the computation over several GPUs, will further enhance the frequency range that can be investigated within reasonable times.

As mentioned above, performing the Schuster periodogram reconstruction up to f_{Ny} is computationally intractable, so we have to reduce the range of frequencies explored. However, for experimental investigations, a first, coarse, estimation of the oscillation frequency is usually possible from first principles (e.g. for STVOs this first estimation can be performed by means of a spectrum analyzer[20]). In the case reported in this work, the excitation frequency is known to be between 58 and 59 MHz, so we performed a first Schuster periodogram calculation between 58 and 60 MHz, shown in Fig. 3(a). The periodogram was calculated for each of the 400 pixels of the image, and the result shown in Fig. 3(a) is their sum for each frequency.

In order to reduce the computation time requested to obtain this first, coarse, periodogram, a frequency step of 20 Hz was employed in the calculation, performed for each frequency according to Eq. (2). To ensure that, even with a 20 Hz frequency step, the two dynamics peaks were visible, only a subset of the recorded arrival times, corresponding to an effective pixel dwell time of 12.5 ms, was used, giving rise to peaks wider than 30 Hz, as shown in Fig. 4. In order to reduce the noise on the periodogram reconstruction, allowing for the identification of weaker amplitude peaks, the periodogram shown in Fig. 3(a) was calculated by averaging 6 periodograms obtained with different subsets of the data, all of which corresponding to an effective pixel dwell time of 12.5 ms.

As shown in Fig. 3(a), four peaks clearly rise above 4 standard deviations of the noise of the periodogram. Two of those peaks, occurring at frequencies of 58.2924 MHz and 59.3333 MHz (marked by the red arrows in Fig. 3(a)) are caused by aliases of the periodogram peak

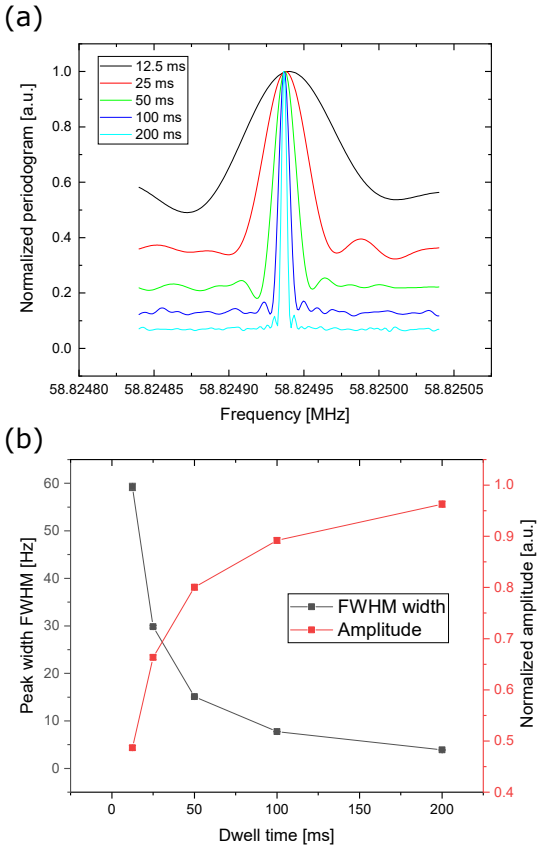

Figure 4: Influence of the pixel dwell time on the width of the periodogram peaks. (a) Plot of the 58.825 MHz peak with different pixel dwell times. The peaks were normalized to their maximum value. (b) Determination of the full width at half maximum (FWHM) of the periodogram peak as a function of the pixel dwell time, showing the expected inverse proportionality. Here, it is also possible to observe that, as expected, the signal to noise ratio improves with a longer pixel dwell time.

occurring at a frequency of 1.0409 MHz. This peak and its aliases are present independently of whether dynamics are excited on the sample or not. The origin of the 1.0409 MHz peak is to be attributed to the filling pattern of the SLS, composed of 420 filled and 60 unfilled electron bunches each separated by 2.0014 ns, which has the consequence that the X-ray illumination of the sample is itself a time-resolved signal with a frequency of 1.0409 MHz. Therefore, the periodogram peaks occurring at multiples of 1.0409 MHz should be discarded. The other two peaks, marked by the black arrows in Fig. 3(a), are, instead, to be attributed to the dynamics occurring in the sample. We therefore performed a second, finer (frequency step of 1 Hz) Schuster periodogram centered around the frequencies of these two peaks using the full dataset (i.e. 200 ms pixel dwell time), the result of which is shown in Fig. 3(b). Here, two clear peaks rise above the noise floor, corresponding to frequencies of 58,500,710 and 58,824,937 Hz (from now on referred to as 58.5 and 58.825 MHz). The ratio between the amplitude of the two peaks is of 3.6 (compared to a ratio of 4 between the power of the two signals), demonstrating that the height of the periodogram peaks reproduces the power of the magnetic excitations.

The data shown in Fig. 3 is the sum of all of the periodograms calculated from each pixel of the TR-STXM image. If we depict the amplitude of the periodogram at each pixel of the image at the two frequencies of 58.5 and 58.825 MHz, it is possible to obtain a spatially resolved map of the amplitude of the magnetization dynamics at the two frequencies. This is shown in the inset of Fig. 3(b), where the same X shape (indicating the motion of the magnetic domain walls in the Landau flux closure pattern that occurs when the vortex gyration mode is excited) observed with the standard reconstruction shown in Fig. 2(c) can be observed. This result shows that the Schuster periodogram can be used to reconstruct a spatially resolved map of the microscopic dynamics in a sample without prior knowledge of its exact oscillation frequency. This statement is also verified by plotting the spatially resolved periodogram amplitude at frequencies outside of the two peaks, where only noise is visible (shown as well in the inset of Fig. 3(b)).

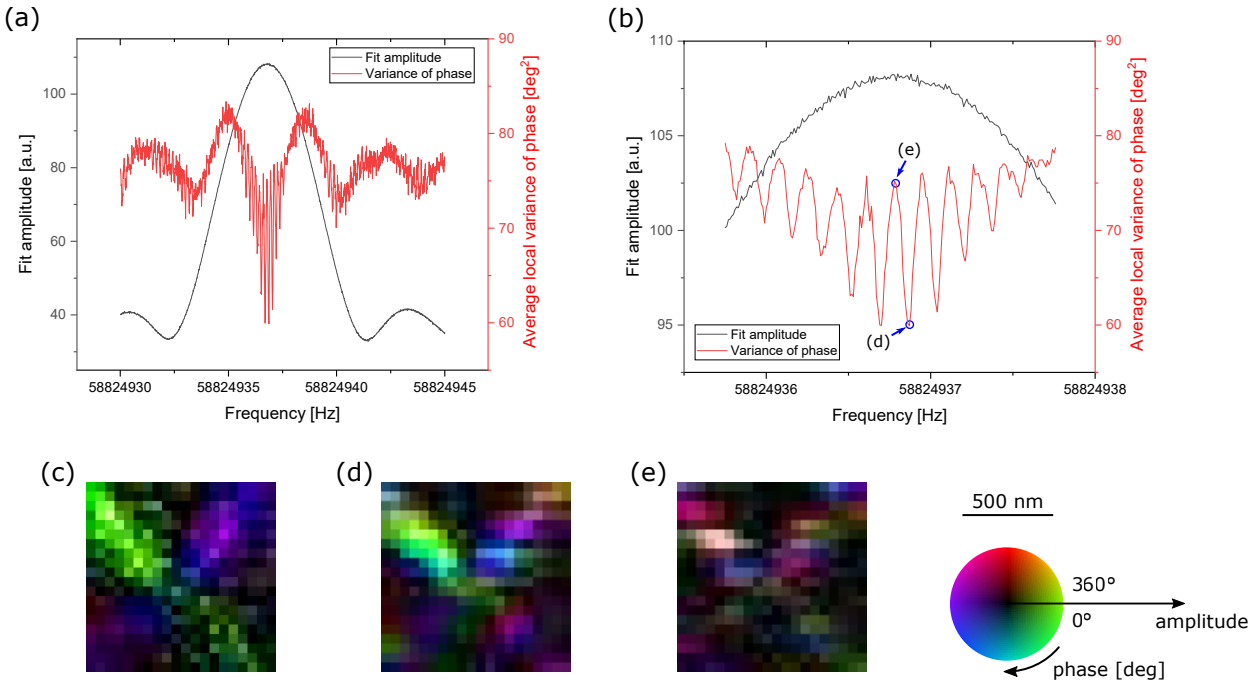

Figure 5: Reconstruction of the phase information. (a) Average amplitude and local spatial variance of the phase around the frequency of 58.825 MHz determined by the Schuster periodogram (calculation details provided in the supplementary information). (b) Same as (a) but zoomed in the region of the maximum amplitude. (c) The phase of the recorded dynamics (with respect to the marker signal) for the standard reconstruction method. (d) The phase of the reconstructed dynamics at the frequency corresponding to the minimum of the average local variance of the phase. (e) The phase of the reconstructed dynamics at the frequency corresponding to one of the local maxima of the average local variance of the phase. The phase in (c-d) is depicted with a HSV color scale, where the hue indicates the value of the phase, between 0 and 360 degrees, and the saturation depicts the amplitude.

The Schuster periodogram allows only for the reconstruction of the amplitude of the magneto-dynamical processes, i.e. the phase information of the dynamical process cannot be reconstructed. However, for the full investigation of the magneto-dynamical processes, the phase information is also of vital importance, e.g. for the reconstruction of the wavelength of spin-waves in magnonic processes[21].

For standard applications of the Schuster periodogram, once the oscillation frequencies of the system under investigation have been identified, the data is then fitted with a sinusoidal fit with its frequency fixed to the one determined by the periodogram[19]. This allows for the determination of the phase of the underlying signal. The same approach can be attempted for the determination of the oscillation phase in the TR-STXM images, by binning the recorded photon arrival times to a "marker" signal with a period corresponding to the frequencies determined by the periodogram. However, due to the fact that a TR-STXM image requires several minutes to be completed and that the oscillation frequencies of the dynamical processes under investigation are on the order of several MHz and above, a small error in the frequency of the "marker" signal leads to a propagating error in the binning of the recorded timestamps, which leads to a faulty reconstruction of the TR image. This is shown in the video included in the supplementary information, where it is possible to recognize that a dynamical process is occurring in the domain walls, but the phase information of such process is not properly reconstructed.

To amend this issue, we performed a reconstruction of the TR image around the frequency determined by the Schuster periodogram with a frequency step of 10 mHz. For each of the attempted frequencies, each pixel was fitted with a sinusoid to determine the amplitude and phase of the oscillation. As metric to determine the best frequency for the reconstruction of the dynamics, we calculated the average local (spatial) variance of the reconstructed phase. This was determined by calculating, for each pixel in the image, the variance of the reconstructed phase of the neighboring pixels, and averaging it over the entire image. Further details on this calculation are given in the supplementary information. The results

of this calculation are shown in Fig. 5(a-b), and the physical motivation for using this figure of merit can be explained by noting that, for the physical process we are investigating, a smooth spatial variation of the phase of the dynamical process can be expected to occur, as shown in Fig. 5(c), where the phase of the vortex gyration process determined from the standard reconstruction method shown in Fig. 2 is shown.

Fig. 5(d) and (e) show two examples of the reconstructed phase of the dynamical oscillation with and without phase optimization (i.e. at the minimum and maximum of the average local variance of the fitted phase - see the supplementary information for the corresponding movies). While a perfect reconstruction of the phase information (i.e. the one performed with the standard method - Fig. 5(c)) will not be possible, due to the lack of information on potential shifts in the phase or the frequency of the excitation signal generated by the AWG, it is sill possible to obtain a reasonable resemblance of the phase information through the minimization of the local spatial variance of the reconstructed phase, as shown in Fig. 5(d). Instead, if a maximum of the local spatial variance of the reconstructed phase is chosen, as in Fig. 5(e), no resemblance can be observed, providing a proof that the minimization the local variance of the reconstructed phase can be used to provide a sufficiently precise estimation of the excitation frequency to allow for the reconstruction of both amplitude and phase of the TR image. Note that the oscillations of the average local variance of the fitted phase are caused by a beating effect between the pixel dwell time and the frequency of the dynamical process occurring in the sample, as detailed in the supplementary information.

The phase reconstruction algorithm described in the paragraphs above is however based on the assumption that the dynamical process under investigation exhibits a stable phase across the entire measurement time, as each time stamp is fitted to a common sinusoidal function (i.e. the fitting is performed to the time difference between the current timestamp and the absolute first timestamp recorded in the image). For dynamical processes exhibiting phase instabilities occurring over timescales less than the entire image measurement time, the assumption described above will not be valid, and the phase reconstruction algorithm cannot

be used. Nonetheless, it is still possible to use the periodogram reconstruction for determining the spatially resolved amplitude of the dynamics, even when the phase instabilities occur at timescales comparable to or below the pixel dwell time (see the supplementary information for additional details).

Conclusions

In conclusion, we have presented a TR microscopy method for the reconstruction of dynamical processes at *a-priori* unknown frequencies. This method applies an algorithm originally developed at the turn of the 19$^{\text{th}}$ century for the determination of oscillation frequencies at the extremely macroscopic scale of astronomical phenomena from scarce, non-uniform, sampling datasets[18]. In our work, we expanded the Schuster periodogram method to be applicable in the nanoscopic world, in particular to scanning probe microscopy, where we can employ it for the reconstruction of both the frequency of dynamical processes and for the spatially resolved determination of the amplitude of the oscillation at these frequencies. We demonstrated the feasibility of the Schuster periodogram reconstruction in a micromagnetic system, where two different, unknown, frequencies were used to excite the gyration of a magnetic vortex core. The Schuster periodogram was able to reconstruct both frequencies, and to determine the ratio between the powers of the two signals. Finally, we show a method, based on the minimization of the local variance of the phase of the oscillation, for providing an estimate of the spatially-resolved phase of the dynamical processes.

With this method, it will be possible to perform TR imaging at the nanoscale of non-locked dynamics such as e.g. auto-oscillation processes, auto-motion processes, and spontaneously forming populations such as condensates. Furthermore, as this setup can be combined with imaging protocols such as three-dimensional TR imaging[22], the ensemble of experimental systems that can be imaged with TR-STXM will be greatly extended, allowing for the investigation of exotic dynamical behaviors in complex sample systems.

Methods

A 2×2 μm^2 area, 150 nm thick, microstructured Py element was fabricated by electron beam lithography followed by liftoff. On top of the microstructured Py square, a 5 μm wide, 400 nm thick, Cu stripline was fabricated using the same method. Further details about the sample fabrication are provided in the supporting information. The Cu stripline was employed to generate an oscillating in-plane magnetic field used to excite the gyration of the magnetic vortex state stabilized in the Py microstructured square. The oscillating magnetic field was generated by injecting an oscillating electrical current across the Cu stripline.

The Py microstructured squares were imaged with the TR-STXM setup of the PolLux beamline of the Swiss Light Source[6], as described above. In order to visualize the magnetic configuration of the Py microstructure, circularly-polarized X-ray photons tuned to the Fe L_3 edge (ca. 707 eV) were employed. The X-ray beam was focused to a spot of 25-30 nm diameter by means of a diffractive Fresnel Zone Plate, and the intensity transmitted across the sample was recorded with an APD. To obtain an image, the sample was raster scanned with a piezoelectric stage. As described above, the absolute timestamp of each photon count at the APD is recorded using a time-to-digital converter (see Fig. 1 for a schematic of the time-of-arrival measurement setup).

To extract the oscillation frequencies of the dynamical processes occurring in the Py microstructure, the recorded photon arrival timestamps were processed, for each pixel of the TR-STXM image, according to Eq. (2) over a defined frequency range and step (in our case, 58-60 MHz with a step of 20 Hz for the coarse periodogram reconstruction - using a subset of the data selected in order to guarantee that the periodogram peaks are wider than the selected 20 Hz step - and over a 1 kHz range with a 1 Hz step around the peaks discovered in the coarse periodogram reconstruction). The processing was performed using a dedicated CUDA script operating on a NVidia GTX 1080 Ti GPU.

Competing Interests

The authors declare no competing financial interests.

Acknowledgement

This work was performed at the PolLux (X07DA) beamline of the Swiss Light Source. The PolLux endstation was financed by the German Bundesministerium für Bildung und Forschung through contracts 05K16WED and 05K19WE2. The authors acknowledge funding from the European Research Council through the ERC HERO-810451 grant.

Supporting Information Available

The following supporting information is available:

- **Supporting_Information.pdf** - Supporting information detailing the sample fabrication, experimental geometry, calculations performed for the results shown in Fig. 5, and the origin of the observed oscillations in the average local variance of the reconstructed phase.

- **standard_reconstruction.avi** - Video showing the vortex gyration dynamics reconstructed with the standard time-resolved imaging method

- **periodogram_goodPhase.avi** - Video showing the vortex gyration dynamics reconstructed with the phase retrieval method shown in Fig. 5. This image corresponds to the phase retrieved in Fig. 5(d)

- **periodogram_badPhase.avi** - Video showing the vortex gyration dynamics reconstructed with the phase retrieval method shown in Fig. 5. This image corresponds to the phase retrieved in Fig. 5(e)

References

(1) Schütz, G.; Wagner, W.; Wilhelm, W.; Kienle, P.; Zeller, R.; Frahm, R.; Materlik, G. Absorption of circularly polarized x rays in iron. *Physical Review Letters* **1987**, *58*, 737.

(2) Baumgartner, M.; Garello, K.; Mendil, J.; Avci, C. O.; Grimaldi, E.; Murer, C.; Feng, J.; Gabureac, M.; Stamm, C.; Ackermann, Y.; Finizio, S.; Wintz, S.; Raabe, J.; Gambardella, P. Spatially and time-resolved magnetization dynamics driven by spin-orbit torques. *Nature Nanotechnology* **2017**, *12*, 980.

(3) Finizio, S.; Zeissler, K.; Wintz, S.; Mayr, S.; Weßels, T.; Huxtable, A. J.; Burnell, G.; Marrows, C. H.; Raabe, J. Deterministic field-free skyrmion nucleation at a nano-engineered injector device. *Nano Letters* **2019**, *19*, 7246.

(4) Bisig, A.; Stärk, M.; Mawass, M.-A.; Moutafis, C.; Rhensius, J.; Heidler, J.; Büttner, F.; Noske, M.; Weigand, M.; Eisebitt, S.; Tylizczak, T.; Van Waeyenberge, B.; Stoll, H.; Schütz, G.; Kläui, M. Correlation between spin structure oscillations and domain wall velocities. *Nature Communications* **2013**, *4*, 2328.

(5) Wintz, S.; Tiberkevich, V.; Weigand, M.; Raabe, J.; Lindner, J.; Erbe, A.; Slavin, A.; Fassbender, J. Magnetic vortex cores as tunable spin-wave emitters. *Nature Nanotechnology* **2016**, *11*, 948.

(6) Raabe, J.; Tzvetkov, G.; Flechsig, U.; Böge, M.; Jaggi, A.; Sarafimov, B.; Vernooij, M. G. C.; Huthwelker, T.; Ade, H.; Kilcoyne, D.; Tyliszczak, T.; Fink, R. H.; Quitmann, C. PolLux: A new facility for soft x-ray Spectromicroscopy at the Swiss Light Source. *Review of Scientific Instruments* **2008**, *79*, 113704.

(7) Puzic, A.; Korhonen, T.; Kalantari, B.; Raabe, J.; Quitmann, C.; Jüllig, P.; Bommer, L.; Goll, D.; Schütz, G.; Wintz, S.; Strache, T.; Körner, M.; Marko, D.; Bunce, C.; Fassbender, J. Photon Counting System for Time-resolved Experiments in Multibunch mode. *Synchrotron Radiation News* **2010**, *23*, 26.

(8) Finizio, S.; Mayr, S.; Raabe, J. Time-of-arrival detection for time-resolved scanning transmission X-ray microscopy imaging. *Journal of Synchrotron Radiation* **2020**, *27*, 1320.

(9) Hubert, A.; Schäfer, R. *Magnetic Domains: The Analysis of Magnetic Microstructures*; Springer Verlag: Heidelberg, 1998.

(10) Raabe, J.; Quitmann, C.; Back, C. H.; Nolting, F.; Johnson, S.; Buehler, C. Quantitative Analysis of Magnetic Excitations in Landau Flux-Closure Structures Using Synchrotron-Radiation Microscopy. *Physical Review Letters* **2005**, *94*, 217204.

(11) Locatelli, N.; Cros, V.; Grollier, J. Spin-torque building blocks. *Nature Materials* **2014**, *13*, 11.

(12) Demokritov, S. O.; Demidov, V. E.; Dzyapko, O.; Melkov, G. A.; Serga, A. A.; Hillebrands, B.; Slavin, A. N. Bose-Einstein condensation of quasi-equilibrium magnons at room temperature under pumping. *Nature* **2006**, *443*, 430.

(13) Barman, A. et al. The 2021 Magnonics Roadmap. *Journal of Physics: Condensed Matter* **2021**, *33*, 413001.

(14) Mohseni, M.; Vasyuchka, V. I.; Lvov, V. S.; Serga, A. A.; Hillebrands, B. Classical analog of qubit logic based on a magnon Bose-Einstein condensate. *Communications Physics* **2022**, *5*, 196.

(15) Frey, P.; Vasyuchka, V. I.; Serga, A. A. Wavevector-dependent magnon accumulation in parametrically populated magnon-phonon spectrum. *Journal of Magnetism and Magnetic Materials* **2021**, *545*, 168628.

(16) Lomb, N. R. Least-squares frequency analysis of unequally spaced data. *Astrophysics and Space Science* **1976**, *39*, 447–462.

(17) Scargle, J. D. Studies in astronomical time series analysis. II. Statistical aspects of spectral analysis of unevenly spaced data. *Astrophysics Journal* **1982**, *263*, 835.

(18) Schuster, A. On the investigation of hidden periodicities with application to a supposed 26 day period of meteorological phenomena. *Terrestrial Magnetism (Journal of Geophysical Research)* **1898**, *3*, 13.

(19) VanderPlas, J. T. Understanding the Lomb–Scargle Periodogram. *The Astrophysical Journal Supplement Series* **2018**, *236*, 16.

(20) Pufall, M. R.; Rippard, W. H.; Kaka, S.; Silva, T. J.; Russek, S. E. Frequency modulation of spin-transfer oscillators. *Applied Physics Letters* **2005**, *86*, 082506.

(21) Träger, N.; Gruszecki, P.; Lisiecki, F.; Groß, F.; Förster, J.; Weigand, M.; Głowiński, H.; Kuświk, P.; Dubowik, J.; Schütz, G.; Krawczyk, M.; Gräfe, J. Real-Space Observation of Magnon Interaction with Driven Space-Time Crystals. *Physical Review Letters* **2021**, *126*, 057201.

(22) Finizio, S.; Donnelly, C.; Mayr, S.; Hrabec, A.; Raabe, J. Three-dimensional resonant magnetization dynamics unraveled by time-resolved soft X-ray laminography. *Nano Letters* **2022**, *22*, 1971.